



New insight into the adsorption of ruthenium, rhodium, and palladium from nitric acid solution by a silica-polymer adsorbent

Shi-Chang Zhang¹ · Shun-Yan Ning¹ · Jie Zhou¹ · Si-Yi Wang¹ · Wei Zhang¹ · Xin-Peng Wang¹ · Yue-Zhou Wei^{1,2}

Received: 3 January 2020 / Revised: 4 February 2020 / Accepted: 10 February 2020 / Published online: 17 March 2020
© China Science Publishing & Media Ltd. (Science Press), Shanghai Institute of Applied Physics, the Chinese Academy of Sciences, Chinese Nuclear Society and Springer Nature Singapore Pte Ltd. 2020

Abstract A porous silica-polymer-based adsorbent, *iso*Bu-BTP/SiO₂-P, was prepared by a vacuum impregnation method and used for the recovery of ruthenium, rhodium, and palladium from nitric acid solution. The experimental results revealed that *iso*Bu-BTP/SiO₂-P exhibited unique adsorption properties such as high saturation adsorption capacity (Ru: 0.35 mmol g⁻¹, Rh: 0.32 mmol g⁻¹, Pd: 1.05 mmol g⁻¹) and excellent selectivity over other metal ions, such as lanthanides (SF_{PGM/M} > 40) in 1 M HNO₃ solution. The adsorption process conformed to the pseudo-second-order model and Langmuir model. From the UV, FTIR, and XPS analyses, it can be concluded that the strong affinity between functional groups (C=N=C) and metal ions as well as NO₃⁻ played a role in coordination during the adsorption process. Furthermore, the desorption behavior was studied, and it was found that the adsorbed Pd, Rh, and Ru could be eluted with a 0.01 M nitric acid–0.1 M thiocarbamide solution, 5 M hydrochloric acid, and sodium hypochlorite (CP) solution, respectively. Finally, based on those findings, a simple process for the separation

and recovery of Pd, Rh, and Ru from high-level liquid waste using *iso*Bu-BTP/SiO₂-P was designed and proposed.

Keywords BTP · Adsorption · Ruthenium · Rhodium · Palladium · High-level liquid waste

Abbreviations

<i>iso</i> Bu-BTP/	2,6-Di(5,6-diisobutyl-1,2,4-triazine-3-
SiO ₂ -P	yl)pyridine
PGMs	Platinum group metals
HLLW	High-level liquid waste
<i>C</i>	Equilibrium ions concentration
<i>m</i>	Mass of the adsorbent
<i>V</i>	Volume of the aqueous phase
<i>E</i>	Adsorption efficiency
<i>K_d</i>	Distribution coefficient
<i>SF</i>	Separation factor
<i>t</i>	Contact time
<i>Q_e</i>	Equilibrium adsorption capacity
<i>Q_t</i>	Adsorption capacity at time <i>t</i>
<i>k₁</i>	Pseudo-first-order constant
<i>k₂</i>	Pseudo-second-order constant
<i>K_L</i>	Langmuir isotherm model constant
<i>K_F</i>	Freundlich isotherm model constant
<i>T</i>	Temperature
<i>C_e</i>	Equilibrium ions concentration
<i>q_m</i>	Calculated saturation adsorption capacity
<i>n</i>	Adsorption intensity
ΔG°	Gibbs free energy
ΔH°	Enthalpy
ΔS°	Entropy
<i>Q_d</i>	Desorption amount

This work was supported by the National Natural Science Foundation of China (Nos. 11705032, 11675102, and 11975082), the Natural Science Foundation of Guangxi Province (No. 2017GXNSFBA198175), and the Science and Technology Major Project of Guangxi Province (No. AA17204100).

✉ Shun-Yan Ning
ningshunyan@gxu.edu.cn

¹ Guangxi Key Laboratory of Processing for Non-ferrous Metals and Featured Materials, School of Resources, Environment and Materials, Guangxi University, Nanning 530004, China

² School of Nuclear Science and Engineering, Shanghai Jiao Tong University, Shanghai 200240, China

C_d	Concentration of adsorbed metal ions in the eluent
E_d	Desorption efficiency

1 Introduction

The platinum group metals (PGMs: Ru, Rh, Pd, Os, Pt, and Ir) have unique properties in many industrial applications, e.g., the aerospace materials, automobile and electroplating industries [1]. However, the abundance of PGMs in the earth's crust is very low, ranging from 0.022 to 0.52 $\mu\text{g L}^{-1}$ [2, 3]. On the other hand, high-level liquid waste (HLLW) contains significant quantities of PGMs, mainly Ru, Rh, and Pd. One ton of spent fuel from a commercial light water reactor or fast breeder reactor contains approximately 4 kg and 19 kg PGMs, respectively. Thus, those spent fuels can be regarded as important PGM sources, comparable with the PGM reserves in the earth [4]. In addition, Ru is easily oxidized to RuO_4 at high temperature; some of this Ru is radiotoxic, such as ^{106}Ru ($t_{1/2}$: 373.6 days), which will enlarge the area contaminated with radioactive waste. Some Ru is coextracted with uranium and plutonium in the plutonium–uranium extraction (PUREX) process; the coextracted Ru is difficult to strip and will reduce the decontamination coefficients of uranium and plutonium, which may interfere with the PUREX process. In addition, the ^{107}Pd content of spent fuel is approximately 0.17 kg ton^{-1} ; this isotope has a half-life of approximately 6.5×10^6 years. Furthermore, during the vitrification process, PGMs increase the glass melting point and phase separation, resulting in uneven distribution of the glass matrix [5–7]. Thus, from the viewpoints of resource recovery, radiotoxicity reduction, and enhancement of the PUREX and vitrification processes, the removal of PGMs from HLLW is crucial. However, the PGM separation process is complicated and costly owing to the high radioactivity, acidity, and complexity of HLLW. Therefore, the question of how to effectively separate and recover PGMs from nitric solution has been receiving increasing attention [8–10].

Many methods have been applied to recover PGMs from HNO_3 solution. Lee et al. [11] studied several ion-exchange resins for the recovery of Ru and Pd from simulated radioactive liquid waste; the resins exhibited excellent adsorption properties. Ozawa et al. [12] proposed the use of ion-exchange chromatography and catalytic electrode hybrid extraction technology to separate PGMs from nitric acid solution. Zambrzycka et al. [13] synthesized a novel ion-imprinted polymer (Ru–BnTsn) that exhibits excellent adsorption performance toward Ru(III) at pH 8.0 ± 0.1 ,

from which Ru can be eluted by 0.3 M thiourea in 0.3 M hydrochloric acid solution. However, previous works have shown very poor efficiency in the separation of PGMs from other metals; this has attracted widespread attention to this subject.

R-BTP ligands are well known for the separation of minor actinides from HLLW. Some studies have found that R-BTPs also have excellent Pd separation ability [14–17]. Ning et al. [14] used $\text{Me}_2\text{-CA-BTP/SiO}_2\text{-P}$ for the effective separation of minor actinides (Am, Cm, etc.) from HLLW and simultaneously realized the separation of Pd and other fission products. Ruiqin Liu used *iso*Hex-BTP/ $\text{SiO}_2\text{-P}$ for the recovery of Pd from 3 M HNO_3 solution with an adsorption capacity of over 0.8 mmol g^{-1} [18]. However, no research has found BTP ligands exhibit good adsorption properties toward Ru and Rh in nitric acid solution. Occasionally, *iso*Bu-BTP/ $\text{SiO}_2\text{-P}$ has been reported to exhibit good adsorption properties toward Ru and Rh at high temperatures, such as 328 K.

Based on the above considerations, the porous material *iso*Bu-BTP/ $\text{SiO}_2\text{-P}$ (Fig. 1) was prepared to separate PGMs from nitric solution [19]. The effect of the HNO_3 concentration, temperature, contact time, and initial PGM concentration on adsorption was studied using batch experiments. The elution behavior of the loaded PGMs under various conditions was also evaluated. Furthermore, the underlying mechanism of interaction between the as-prepared adsorbent and the PGMs was evaluated by means of spectroscopy (FTIR, XPS) in this study.

2 Experimental section

2.1 Reagents

All reagents, such as nitric acid, hydrochloric acid, perchloric acid, methanol, dichloromethane, and thiourea, were of analytical grade. Stock solutions including those of Ru(III), Rh(III), Pd(II), and other fission products (FPs) were purchased from Aladdin Biochemical Technology Co., Ltd (Shanghai). The purity of *iso*Bu-BTP was 94% according to HPLC tests. *iso*Bu-BTP dissolved in CH_2Cl_2 was loaded into porous $\text{SiO}_2\text{-P}$ with a diameter of approximately 50 μm and a pore size of approximately 60 nm to achieve an *iso*Bu-BTP loading rate of approximately 33 wt% [19].

2.2 Evaluation of adsorption performance

PGM adsorption experiments were carried out using the as-prepared adsorbents; 0.05 g of the adsorbent was mixed with 2.5 mL of liquid containing the targeted metal ions and then shaken mechanically at a constant speed

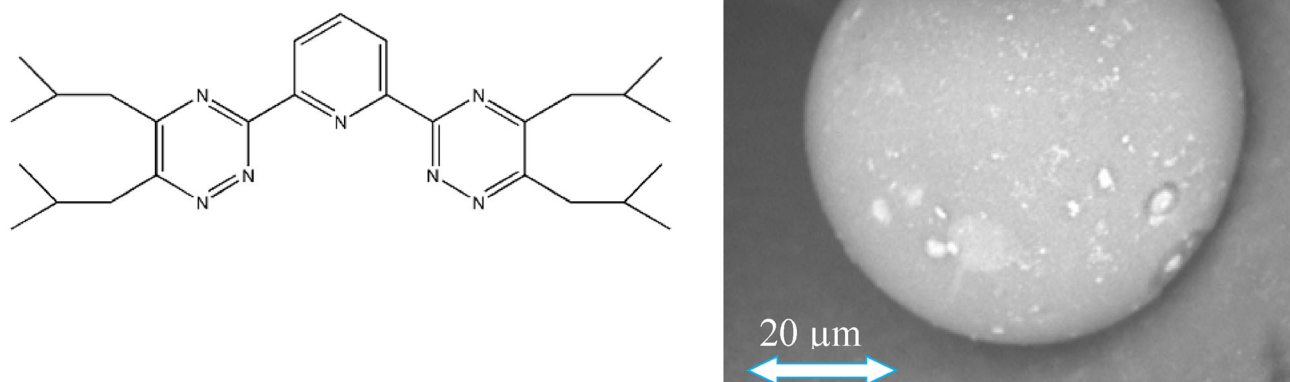


Fig. 1 Structure of *isoBu-BTP* (left) and SEM picture of *isoBu-BTP/SiO₂-P* (right)

(120 rpm). A filter with a pore size of 0.45 μm was used for phase separation. The concentrations of the metal ions in the aqueous solutions were tested using ICP-AES (Shimadzu, ICPS-7510). The adsorption capacity Q (mmol g^{-1}), adsorption efficiency E (%), distribution coefficient K_d (mL g^{-1}), and separation factor SF_{MIN} were calculated as follows:

$$Q = \frac{(C_0 - C)}{m} \times V, \quad (1)$$

$$E = \frac{(C_0 - C)}{C_0} \times 100\%, \quad (2)$$

$$K_d = \frac{(C_0 - C)}{C} \times \frac{V}{m}, \quad (3)$$

$$SF_{M/N} = K_{dM}/K_{dN}, \quad (4)$$

where C_0 and C (mg L^{-1}) are the concentration of the original solution and the concentration at adsorption equilibrium, respectively. V (mL) and m (g) are the volume of the initial solution and the weight of the adsorbent.

2.3 Mechanistic study

UV spectroscopy (UV-3600 Plus, SHIMADZU) was applied to analyze the effect of the H^+ concentration and temperature on the PGM adsorption mechanism of *isoBu-BTP/SiO₂-P*. The analysis of the effect of the H^+ concentration was performed in a mixed solution of acetonitrile/ HClO_4 ($V:V = 1:1$) by fixing the concentration of fresh *isoBu-BTP* (1×10^{-4} M) and varying the HClO_4 concentration. HClO_4 was chosen to adjust the H^+ concentration because ClO_4^- cannot coordinate with the adsorbent, thus eliminating a potential anion effect. To analyze the temperature effect, *isoBu-BTP/SiO₂-P* was first placed in

contact with 1 M HNO_3 at different temperatures for three days. After phase separation and drying in a vacuum oven, the *isoBu-BTP* was dissolved in acetonitrile to achieve a 2×10^{-4} M *isoBu-BTP* concentration.

The changes in the functional groups of fresh *isoBu-BTP/SiO₂-P* and PGM-loaded *isoBu-BTP/SiO₂-P* were characterized by FTIR using an IRTracer-100 instrument (SHIMADZU). The sample was prepared by mixing the *isoBu-BTP/SiO₂-P* with potassium bromide (KBr), fully grinding the resulting mixture, and pressing it into thin sheets.

Furthermore, XPS (Thermo ESCALAB 250XI) was used to analyze chemical changes in the adsorbent before and after adsorption. The C 1s peak was corrected to 284.6 eV. The samples were dried by placing them in a vacuum constant temperature drying oven (VOC-210C, EYELA) at 313 K.

3 Results and discussion

3.1 Batch adsorption experiments

3.1.1 Effects of HNO_3 concentration and temperature

The effect of the HNO_3 concentration at 328 K and that of the temperature on the adsorption behavior of *isoBu-BTP/SiO₂-P* toward the PGMs were evaluated (Fig. 2). The adsorption of the adsorbent toward PGMs first increased with increasing HNO_3 concentration and reached a maximum at 1 M HNO_3 with Pd, Ru, and Rh adsorption efficiencies as high as 99.9%, 96.7%, and 67.4%, respectively, and then decreased with further increase in the HNO_3 concentration (Fig. 2a). Furthermore, the changes in the

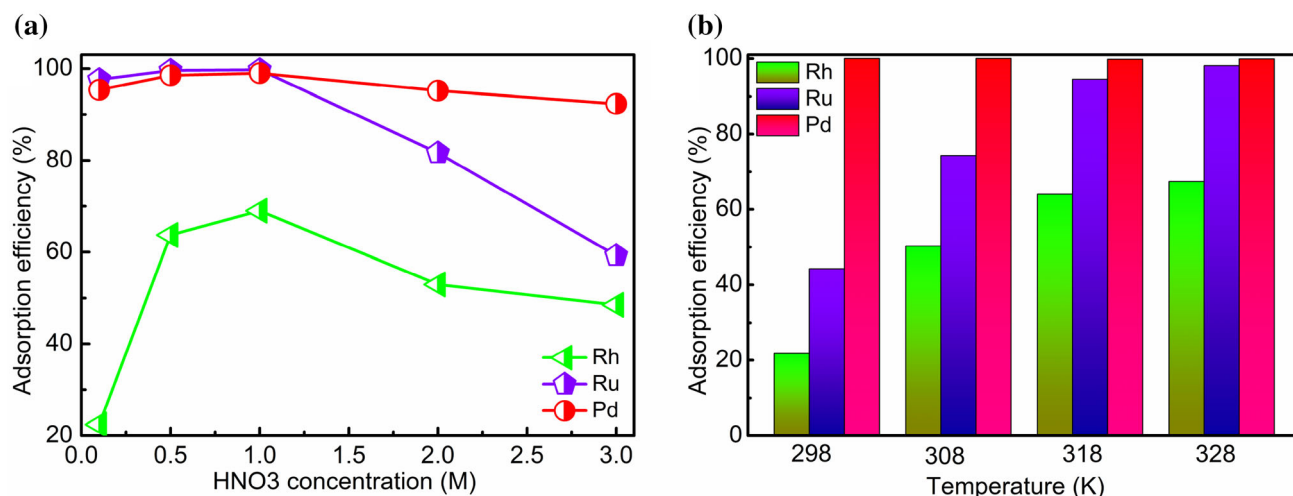


Fig. 2 (Color online) Effect of the initial HNO₃ concentration (328 K) (a) and temperature (b) on the adsorption of PGMs by *iso*Bu-BTP/SiO₂-P ($m/V = 0.02 \text{ g mL}^{-1}$, $C_0: 2 \text{ mmol L}^{-1}$)

adsorption behavior with temperature were also investigated. As the temperature was increased from 298 to 328 K (Fig. 2b), the adsorption efficiency toward Pd(II) exhibited almost no change, while the adsorption efficiency toward Ru(III) and Rh(III) increased rapidly.

UV spectra were used to elucidate the adsorption phenomena caused by temperature and acid (Fig. 3). With increasing H⁺ concentration, an isosbestic point appeared at approximately 305 nm, indicating the generation of a new species which was supposed to be protonated *iso*Bu-BTP/SiO₂-P [20]. The UV absorption intensity increased ($C_{\text{HNO}_3} < 1 \text{ M}$) and then remained stable as the H⁺ concentration was further increased to 2 M (Fig. 3a), indicating that protonated *iso*Bu-BTP/SiO₂-P was gradually formed [20]. It is well known that the dominant form of Pd is Pd²⁺ and that the main forms of Rh are Rh³⁺ and

Rh(NO₃)²⁺, while Ru(III) can exist in the form of complex complexes such as Ru(NO)³⁺ and [RuNO(NO₃)_{*n*}(H₂O)_{5-*n*}]^{3-*n*} in nitric acid solution [2, 11, 21]. The positive charge of the protonated adsorbent would not be beneficial to adsorption of metal ions with positive charges, such as Pd²⁺ and Rh(NO₃)²⁺. Thus, the decrease in adsorption may be caused by the increase in protonation with acidity. However, the overall adsorption process requires NO₃⁻ to maintain charge balance, as was proven later by IR and XPS analysis. This leads to the increase in adsorption with increasing acidity in the 0.1–1 M HNO₃ range. The effect of temperature on the UV spectra of *iso*Bu-BTP/SiO₂-P after contact with 1 M HNO₃ solution at 298–328 K was also studied (Fig. 3b). The absorption intensity of the UV spectra decreased with increasing temperature, which

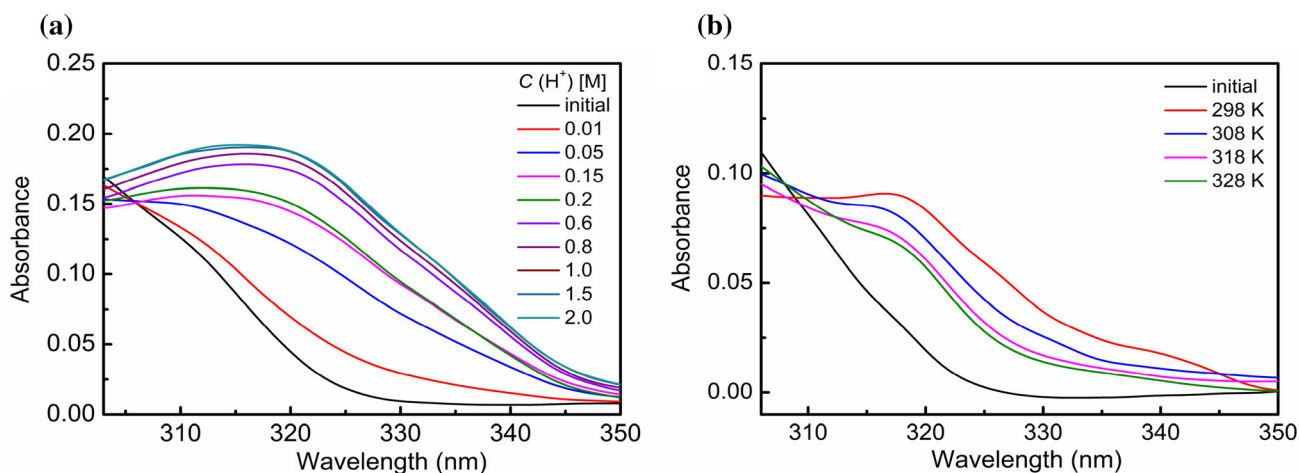


Fig. 3 (Color online) Effect of increasing proton concentration ($C_{\text{adsorbent}} = 1 \times 10^{-4} \text{ mmol L}^{-1}$) (a) and temperature (b) ($C_{\text{HClO}_4} = 1 \text{ mol L}^{-1}$, $C_{\text{adsorbent}} = 2 \times 10^{-4} \text{ mmol L}^{-1}$) on the UV spectra of *iso*Bu-BTP/SiO₂-P in H₂O-acetonitrile (1:1)

indicates a decreased degree of protonation that resulted in the increase in adsorption with temperature [20, 22, 23].

Moreover, the adsorption behavior of the adsorbent toward other elements that are usually present in HLLW, such as Sr, Zr, Mo, Y, La, Ce, Pr, Nd, Sm, Eu, and Gd, was studied at 328 K (Fig. 4). The K_d values of the PGMs were much higher than those of the other metal ions, with an $SF_{\text{PGMs}/M}$ value of over 40, indicating that Ru, Rh, and Pd could be effectively and efficiently separated from other metal ions using *iso*Bu-BTP/SiO₂-P.

3.1.2 Kinetics study

The kinetics of PGM adsorption at various temperatures was studied (Fig. 5). The adsorption of Ru(III) (Fig. 5a) was relatively slow at 298 K, and with the uptake rate still increasing at a contact time of 144 h. The adsorption kinetics was significantly improved at higher temperatures, and equilibrium was obtained within approximately two days at 318 K and 328 K. In the case of Rh(III) (Fig. 5b), the adsorption kinetics improved with increasing temperature, but a long time was required to reach equilibrium even at 328 K. For Pd(II) (Fig. 5c), adsorption was relatively fast compared with Ru and Rh, with equilibrium being obtained within 1 day.

To clearly understand the adsorption characteristics, both a pseudo-first-order kinetics model (PFORE, Eq. 5) and a pseudo-second-order kinetic model (PSORE, Eq. 6) were employed to analyze the experimental data [24]:

$$\ln(Q_e - Q_t) = \ln Q_e - k_1 t, \quad (5)$$

$$\frac{t}{Q_t} = \frac{1}{k_2 Q_e} + \frac{t}{Q_e}, \quad (6)$$

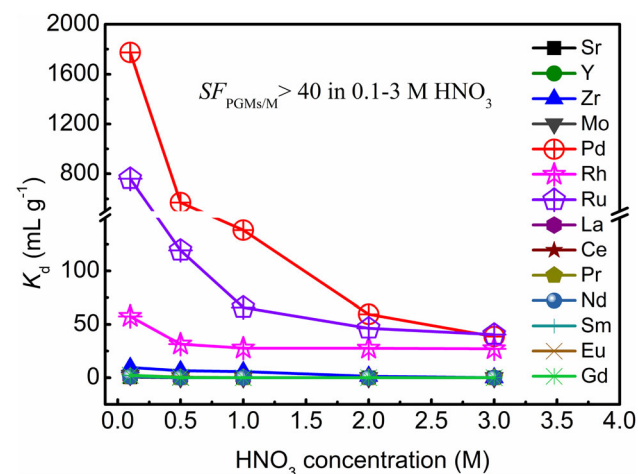


Fig. 4 (Color online) Effect of the initial HNO₃ concentration on the adsorption of PGMs and other metal ions by *iso*Bu-BTP/SiO₂-P ($m/V = 0.02 \text{ g mL}^{-1}$, $C_{\text{PGMs}} = 2 \text{ mmol L}^{-1}$, $C_M = 2 \text{ mmol L}^{-1}$, $T = 328 \text{ K}$)

where Q_t and Q_e (mmol g^{-1}) are the adsorption capacity at t (h) and equilibrium and k_1 (h^{-1}) and k_2 ($\text{mmol g}^{-1} \text{ h}^{-1}$) are the constants of the PFORE and PSORE, respectively.

The fitting results are shown in Table 1 and Fig. 5d for Ru(III), Fig. 5e for Rh(III), and Fig. 5f for Pd(II). As shown in Table 1, based on the higher correlation coefficients (R^2) and excellent consistency between the calculated equilibrium adsorption capacities (Q_e) and the experimental ones ($Q_{e,\text{exp}}$), the experimental results were well fitted by the PSORE model, which indicates that the overall process is mainly chemical adsorption. Moreover, k_2 also increases quickly with temperature, which means that the adsorption rate increases quickly.

3.1.3 Adsorption isotherms

The adsorption isotherms were determined by increasing the initial metal ion concentrations of each PGM individually in solution (Fig. 6). The uptake amount (Q_e) increased with the increase in the PGM equilibrium concentrations. Furthermore, Q_e increased significantly with temperature, which means that increasing temperature is beneficial to adsorption. Both the Langmuir isotherm model and the Freundlich isotherm model shown in Eqs. 7 and 8, respectively, were used to analyze the experimental data [24]:

$$Q_e = \frac{q_m \times K_L \times C_e}{1 + K_L \times C_e}, \quad (7)$$

$$Q_e = K_F \times C_e^{\frac{1}{n}}, \quad (8)$$

where Q_e (mmol g^{-1}) is the equilibrium uptake amount and q_m (mmol g^{-1}), and C_e (mmol L^{-1}) are the calculated saturation adsorption capacity and equilibrium ion concentration in solution, respectively. K_L (L mmol^{-1}) is the Langmuir constant, and K_F ($\text{mmol}^{1-n} \text{ L}^n \text{ g}^{-1}$) and n are the Freundlich constants.

As shown in Table 2, the higher R^2 values and consistency between q_m and $Q_{e,\text{exp}}$ indicate that the adsorption behavior of the PGMs is better fitted with the Langmuir model, which in turn suggests that the overall adsorption process is mainly monolayer chemical adsorption. Compared with other adsorbents (Table 3), the high adsorption capacity is one of the biggest highlights of *iso*Bu-BTP/SiO₂-P.

3.1.4 Adsorption thermodynamics

According to the experimental results, the amount of PGMs adsorbed on *iso*Bu-BTP/SiO₂-P increased with temperature. To better understand the adsorption

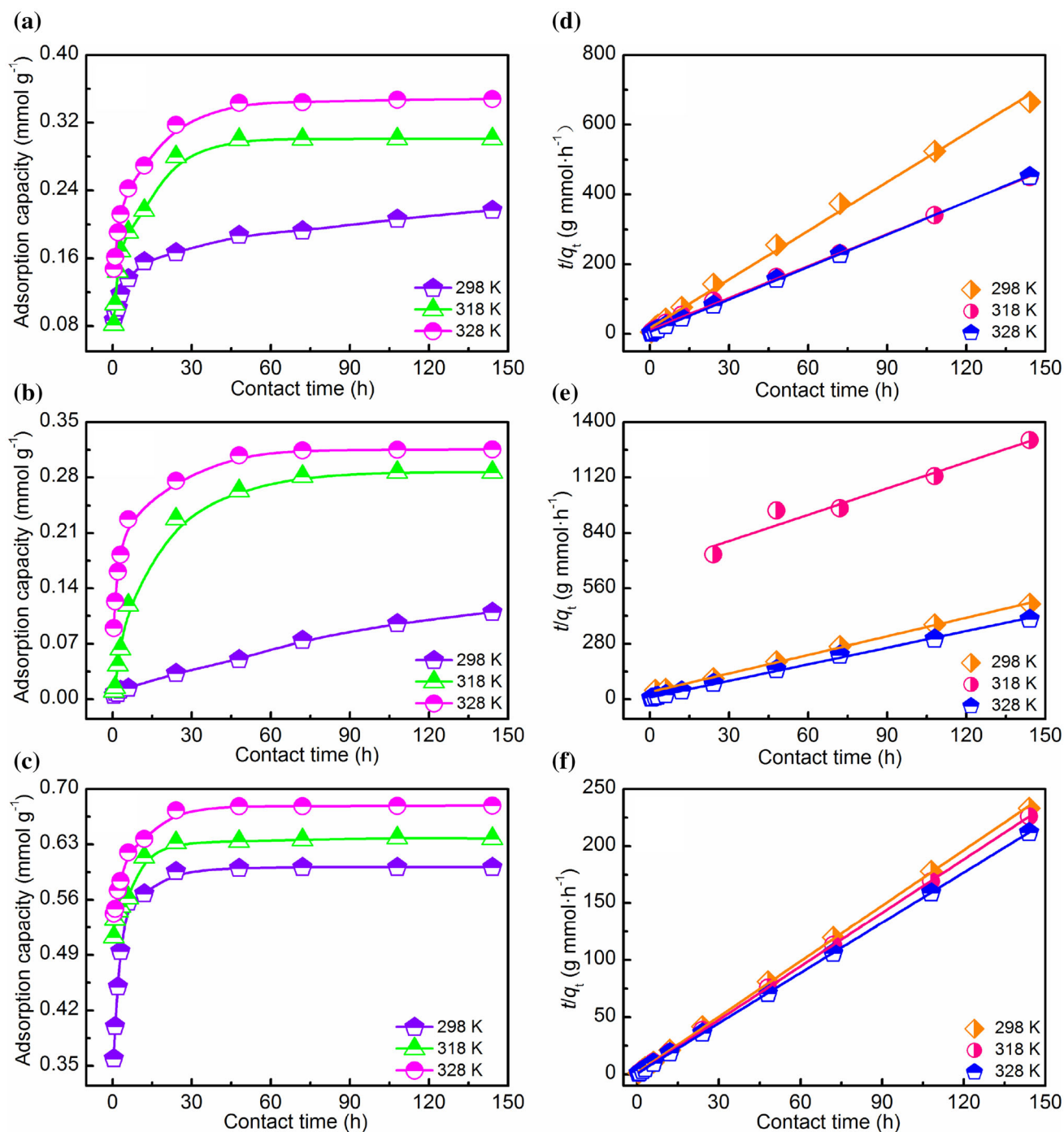


Fig. 5 (Color online) Kinetics of the adsorption of Ru(III) (a), Rh(III) (b), and Pd(II) (c) onto *iso*Bu-BTP/SiO₂-P ($m/V = 0.02 \text{ g mL}^{-1}$, C_{Ru} , C_{Rh} : 10 mmol L^{-1} , C_{Pd} : 15 mmol L^{-1} , C_{HNO_3} : 1 mol L^{-1})

thermodynamics, the main thermodynamic parameters were obtained using the Van't Hoff equation [32]:

$$\ln K_L = -\frac{\Delta H^\circ}{RT} + \frac{\Delta S^\circ}{R}, \quad (9)$$

$$\Delta G^\circ = \Delta H^\circ - \Delta S^\circ T, \quad (10)$$

where ΔG° (J mol^{-1}), ΔH° (J mol^{-1}), and ΔS° ($\text{J K}^{-1} \text{ mol}^{-1}$) are the changes in the Gibbs free energy, enthalpy, and entropy, respectively. R ($8.314 \text{ J K}^{-1} \text{ mol}^{-1}$) represents the gas constant at temperature T (K).

As depicted in Fig. 6d and Table 4, the values of positive ΔH° were positive, which means that the adsorption is endothermic. This is consistent with the observation that

Table 1 PFORE and PSORE kinetic model parameters for the adsorption of the PGMs on *iso*Bu-BTP/SiO₂-P at various temperatures

Element	<i>T</i> (K)	Pseudo-first-order model			Pseudo-second-order model			<i>Q_{e,exp}</i> (mmol g ⁻¹)
		<i>K</i> (h ⁻¹)	<i>Q_e</i> (mmol g ⁻¹)	<i>R</i> ²	<i>K</i> (g mmol h ⁻¹)	<i>Q_e</i> (mmol g ⁻¹)	<i>R</i> ²	
Ru	298	0.48	0.22	0.599	0.27	0.22	0.996	0.22
	318	0.29	0.33	0.804	0.26	0.31	0.998	0.30
	328	0.72	0.32	0.663	0.55	0.35	0.999	0.35
Rh	298	0.01	0.13	0.97	0.007	0.12	0.943	0.12
	318	0.09	0.30	0.98	0.086	0.29	0.999	0.29
	328	0.33	0.33	0.908	0.306	0.32	0.998	0.32
Pd	298	1.34	0.61	0.682	1.02	0.61	1.000	0.62
	318	3.29	0.63	0.282	2.24	0.64	1.000	0.64
	328	3.46	0.67	0.272	2.32	0.68	1.000	0.68

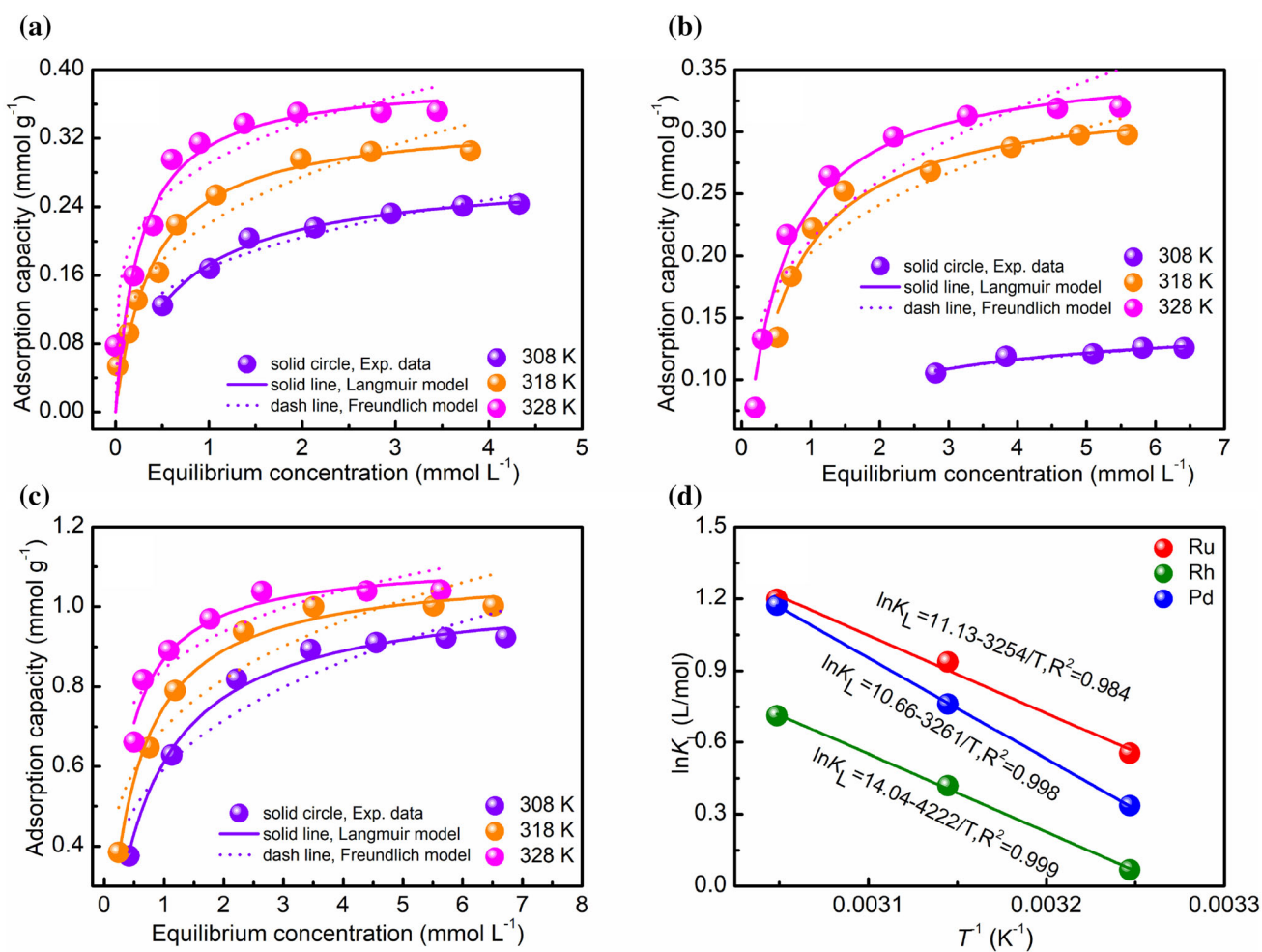


Fig. 6 (Color online) Adsorption isotherms of Ru (a), Rh (b), and Pd (c), and plots of lnK_L versus T⁻¹ (d) (C_{HNO₃} = 1 mol L⁻¹)

Table 2 Adsorption isotherm parameters of the two models for the adsorption of the PGMs on *iso*Bu-BTP/SiO₂-P at 308, 318, and 328 K

Element	<i>T</i> (K)	Langmuir isotherm			Freundlich isotherm			<i>Q</i> _{e,exp} (mmol g ⁻¹)
		<i>K</i> _L (L mmol ⁻¹)	<i>q</i> _m (mmol g ⁻¹)	<i>R</i> ²	<i>n</i>	<i>K</i> _F (mmol ^{1-<i>n</i>} L ^{<i>n</i>} g ⁻¹)	<i>R</i> ²	
Ru	308	1.49	0.25	0.989	4.19	0.18	0.927	0.24
	318	2.42	0.30	0.971	2.85	0.20	0.939	0.31
	328	3.31	0.34	0.893	3.89	0.24	0.819	0.35
Rh	308	0.93	0.14	0.919	4.95	0.09	0.874	0.13
	318	1.81	0.30	0.961	3.83	0.21	0.864	0.30
	328	1.82	0.33	0.982	2.60	0.21	0.855	0.32
Pd	308	1.40	0.91	0.989	3.56	0.57	0.882	0.92
	318	2.14	1.01	0.988	3.73	0.69	0.867	1.00
	328	3.23	1.06	0.944	5.47	0.87	0.792	1.05

Table 3 Comparison of the adsorption *Q*_(Ru, Rh, Pd) of *iso*Bu-BTP/SiO₂-P with those of other materials

	Material	Acid concentration (M)	Temperature (K)	<i>Q</i> (mmol g ⁻¹)	Contact time	Reference
Ru	(Cera + Dodec)/SiO ₂ -P	3 HNO ₃	298	0.088	20 h	[25]
	Lewatit Mono Plus M600	Acetic acid	298	0.048	45 min	[26]
	Raw. <i>C. glutamicum</i> biomass	Acetic acid	298	0.15	30 min	[26]
	This work	1 HNO ₃	328	0.35	48 h	
Rh	(Cera + Dodec)/SiO ₂ -P	3 HNO ₃	298	0.072	72 h	[25]
	(Crea + TOA)/SiO ₂ -P	3 HNO ₃	298	0.306	72 h	[27]
	Purolite S985	2.35 HCl	Room temperature	0.120	24 h	[28]
	This work	1 HNO ₃	328	0.32	48 h	
Pd	Me ₂ -CA-BTP/SiO ₂ -P	3 HNO ₃	298	0.80	12 h	[29]
	XAD-16	3 HNO ₃	298	0.19	45 min	[30]
	<i>iso</i> Hex-BTP/SiO ₂ -P	3 HNO ₃	298	0.89	24 h	[31]
	This work	1 HNO ₃	328	1.05	24 h	

Table 4 Thermodynamic parameters of the adsorption of the PGMs on *iso*Bu-BTP/SiO₂-P

Element	<i>T</i> (K)	<i>K</i> _L (L mol ⁻¹)	ΔH° (J mol ⁻¹)	ΔS° (J mol ⁻¹)	ΔG° (J mol ⁻¹)
Ru	308	1.74 × 10 ³	3.25 × 10 ³	11.13	- 0.18 × 10 ³
	318	2.55 × 10 ³			- 0.29 × 10 ³
	328	3.31 × 10 ³			- 0.40 × 10 ³
Rh	308	1.07 × 10 ³	3.26 × 10 ³	10.66	- 0.02 × 10 ³
	318	1.52 × 10 ³			- 0.13 × 10 ³
	328	2.04 × 10 ³			- 0.24 × 10 ³
Pd	308	1.40 × 10 ³	4.22 × 10 ³	14.04	- 0.10 × 10 ³
	318	2.14 × 10 ³			- 0.24 × 10 ³
	328	3.23 × 10 ³			- 0.39 × 10 ³

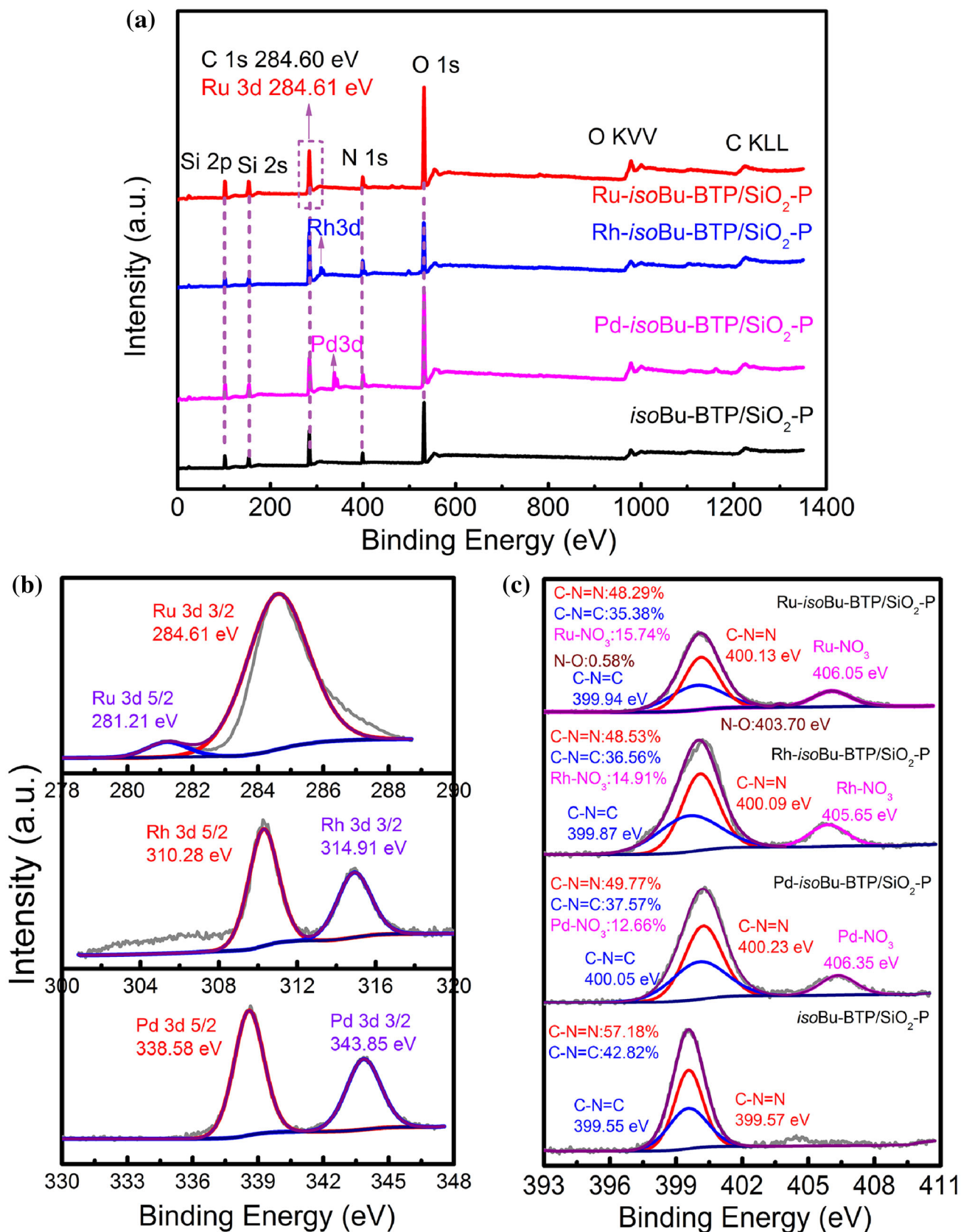


Fig. 7 XPS survey scans of pure *isoBu-BTP/SiO₂-P* and *isoBu-BTP/SiO₂-P* with adsorbed PGMs (a), narrow scans of the adsorbed PGMs (b), and N 1s spectra before and after PGMs adsorption (c)

the saturation adsorption capacity increases with temperature. The negative ΔG° values indicate that the adsorption is spontaneous. Moreover, the positive ΔS° values indicate that the adsorption of PGMs on *iso*Bu-BTP/SiO₂-P is an entropy-driven process.

3.2 Interaction mechanism study

3.2.1 XPS analysis

XPS was employed to obtain more information about the changes to the functional groups and electronic states of *iso*Bu-BTP/SiO₂-P. As depicted in Fig. 7a, the peaks of the four main elements (C, N, O, and Si) are observed in all samples, but the signals of the PGMs are only observed in the PGM-loaded adsorbents, which indicates that the PGMs were adsorbed successfully. The 3D scans of the PGMs are shown in Fig. 7b. The doublet separation between the $3d\ 3/2$ and $3d\ 5/2$ peaks of Ru, Rh, and Pd is 3.4 eV, 4.63 eV, and 5.27 eV, respectively, which fit well with the previously reported results [33–36]. Due to the overlap of C $1s$ (284.6 eV) and Ru $3d\ 3/2$ (284.61 eV), the peak of Ru $3d\ 3/2$ shows a small deviation [37]. The state of N is very complicated. In the case of fresh *iso*Bu-BTP/SiO₂-P (Fig. 7c), only two forms of N are present, i.e., C–N=C and C–N=N. The ratio of C–N=C to C–N=N is 42.82%:57.18%, which is very close to the theoretical ratio of 3:4. For the PGM-loaded *iso*Bu-BTP/SiO₂-P samples, other forms of N may exist, such as N–O in [RuNO] and NO₃[−] complexed with PGMs [33, 38–43]. Furthermore, in the N $1s$ spectra, the binding energy of C–N=C shifts from 399.55 to 399.94 eV (Ru), 399.87 eV (Rh), and 400.05 eV (Pd), and the energy of C–N=N shifts from 399.57 to 400.13 eV (Ru), 400.09 eV (Rh), and 400.23 eV (Pd). These interesting shifts revealed the strong charge

interactions between the PGMs and nitrogen-containing functional groups.

3.2.2 FTIR analysis

FTIR analysis was employed to further understand the interaction mechanism between the as-prepared adsorbent and Ru and Rh (Fig. 8). The characteristic peaks at 1113, 802, 475 cm^{−1} result from the Si–O–Si stretching vibration [15]. The peak at 1379 cm^{−1} is indicative of the C–H bond. In addition, the transmittance was enhanced after the adsorption of the PGMs. The reason for this phenomenon is that NO₃[−] also has a characteristic peak at 1380 cm^{−1} and two peaks (C–H and NO₃[−]) are superimposed [44], which implies that NO₃[−] participates in the adsorption process. The peak at 1635 cm^{−1} arises from the C–N=N of the pyridine ring and shows almost no change after adsorption. The characteristic peak of C–N=C in the pyridine ring exhibits significant shifts, from 1526 to 1552 cm^{−1} after Ru adsorption and 1540 cm^{−1} after Rh adsorption. The two peaks located at the 2870 and 2970 cm^{−1} should arise from the C–H and SiO₂-P of *iso*Bu-BTP, respectively. The peak centered at 3440 cm^{−1} originates from the O–H of H₂O. Comparing the spectra before and after adsorption, almost no significant changes were found except for the significant shift in the position of C–N=C, which implies that the C–N=C (pyridine ring) plays an important role in the overall adsorption process. The larger shift of C–N=C in Ru-*iso*Bu-BTP/SiO₂-P compared to Rh-*iso*Bu-BTP/SiO₂-P indicates stronger interaction between the adsorbent and Ru(III) than Rh(III), which may be attributed to the different ionic radii (Pd²⁺ > Ru³⁺ > Rh³⁺) [45] leading to a better match in terms of size. Moreover, the spectra exhibited almost no changes with increasing time,

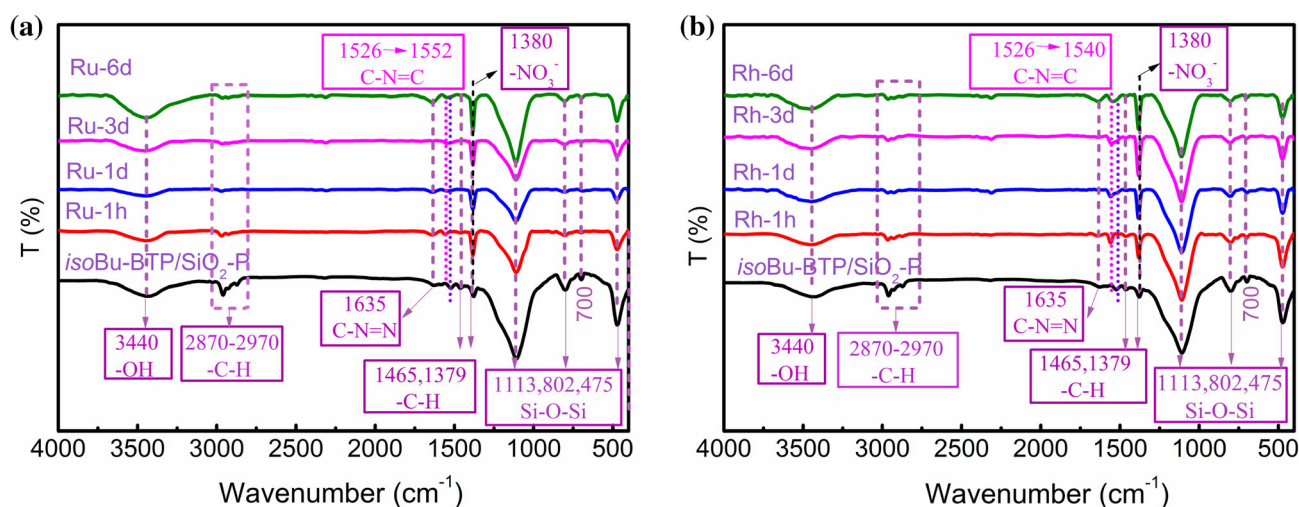


Fig. 8 (Color online) FTIR spectra of the pure adsorbent and the adsorbent after the adsorption of Ru (a) and Rh (b)

indicating that the interaction mechanism did not change over time.

3.3 Desorption performance

To further evaluate the performance of *iso*Bu-BTP/SiO₂-P, the desorption performances of different eluents were evaluated; the results are shown in Table 5. In complex mixed-metal systems, such as HLLW, other metal ions may also be involved, so the desorption behavior of Ln was also studied. The poorly adsorbed lanthanide(III) could be desorbed by all the experimental eluents, so it could be desorbed first using H₂O, which had poor elution performance toward the other metal ions in the desorption stage. In our previous research, it was found that Am(III) could be effectively desorbed using 0.01 M DTPA, which is very

similar to EDTA-2Na and cannot effectively desorb PGMs, after Ln(III) was desorbed by H₂O, [46] which can be desorbed using a by 0.01 M HNO₃–0.1 M thiocarbamide solution but not by water or EDTA-2Na, and could then be eluted. After that, Rh(III) could be desorbed using 5 M HCl. Finally, a NaClO solution is used to desorb Ru(III). A simple process to separate PGMs from simulated HLLW using *iso*Bu-BTP/SiO₂-P is proposed in Fig. 9.

4 Conclusion

In this work, the silica-polymer-based adsorbent *iso*Bu-BTP/SiO₂-P was synthesized for the separation and recovery of palladium, rhodium, and ruthenium from a nitric acid medium. The results show that the adsorbent exhibits superior adsorption properties, with uptake rates of over 98% for Ru, 64% for Rh, and 99% for Pd in 1 M nitric acid solution at 328 K. The adsorption behavior toward the PGMs matched well with the PSORE model, with adsorption equilibrium being obtained within 2d, 3d, and 1d for Ru, Rh, and Pd at 328 K, respectively. Furthermore, the experimental data reveal that the saturation adsorption capacities of the adsorbent toward Ru, Rh, and Pd are 0.35, 0.32, and 1.05 mmol g⁻¹ and fit well with the Langmuir model. Moreover, according to the calculated thermodynamics results, it can be concluded that the whole adsorption process is actually endothermic. FTIR and XPS analyses revealed that nitrogen-containing functional groups (C–N=C) interacted strongly with the metal ions and that NO₃⁻ participated in coordination during adsorption. In addition, the use of different desorption agents in different stages can successfully achieve the desorption and separation of Ln, Am, Pd, Rh, and Ru. Finally, a process for the separation of PGMs from simulated HLLW based on *iso*Bu-BTP/SiO₂-P was proposed. In brief, *iso*Bu-BTP/SiO₂-P has unique advantages in the field of PGM separation and recovery and also has great application prospects in the separation of PGMs from HLLW.

Table 5 Desorption results of the different materials

Eluent	Desorption efficiency (%)			
	Ru	Rh	Pd	Ln
Pure water	2.2	4.7	4.8	89.6
0.01 M HNO ₃ –0.1 M THU	6.1	3.9	90.1	82.5
5 M HCl	6.9	78.4	38.6	85.3
NaClO(CP)	68.6	59.4	75.5	74.1
0.01 M EDTA-2Na	2.4	7.6	5.4	65.4

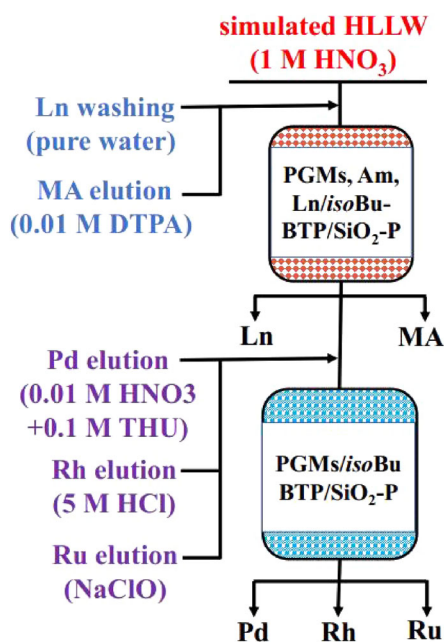


Fig. 9 Process for the separation of Ln, Am, Ru, Rh, and Pd from HLLW based on *iso*Bu-BTP/SiO₂-P

References

1. Y. Yan, Q. Wang, Z. Xiang et al., Separation of Pt(IV), Pd(II), Ru(III), and Rh(III) from chloride medium using liquid–liquid extraction with mixed imidazolium-based ionic liquids. *Sep. Sci. Technol.* **53**, 2064–2073 (2018). <https://doi.org/10.1080/01496395.2018.1440304>
2. P. Swain, C. Mallika, R. Srinivasan et al., Separation and recovery of ruthenium: a review. *J. Radioanal. Nucl. Chem.* **298**, 781–796 (2013). <https://doi.org/10.1007/s10967-013-2536-5>
3. G.M. Mudd, S.M. Jowitt, T.T. Werner, Global platinum group element resources, reserves and mining—a critical assessment.

- Sci. Total Environ. **622**, **623**, 614–625 (2018). <https://doi.org/10.1016/j.scitotenv.2017.11.350>
4. R.P. Bush, Recovery of platinum group metals from high level radioactive waste. *Platin. Met. Rev.* **35**, 202–208 (1991)
 5. P. Swain, S. Annapoorani, R. Srinivasan et al., Separation of ruthenium from simulated nuclear waste in nitric acid medium using n-paraffin hydrocarbon. *Sep. Sci. Technol.* **49**, 112–120 (2013). <https://doi.org/10.1080/01496395.2013.815629>
 6. A. Zhang, L. Xu, G. Lei, Separation and complexation of palladium(II) with a new soft N-donor ligand 6,6'-bis(5,6-dinonyl-1,2,4-triazin-3-yl)-2,2'-bipyridine (C9-BTBP) in nitric acid medium. *New J. Chem.* **40**, 6374–6383 (2016). <https://doi.org/10.1039/c5nj03082j>
 7. K.A. Venkatesan, B.R. Selvan, M.P. Antony et al., Extraction of palladium from nitric acid medium by commercial resins with phosphinic acid, methylene thiol and isothiuronium moieties attached to polystyrene-divinylbenzene. *J. Radioanal. Nucl. Chem.* **266**(3), 431–440 (2005). <https://doi.org/10.1007/s10967-005-0928-x>
 8. S. Liu, Y. Wei, R. Liu et al., Electrochemical behavior and electrowinning of palladium in nitric acid media. *Sci. China Chem.* **56**, 1743–1748 (2013). <https://doi.org/10.1007/s11426-013-4945-2>
 9. S. Gu, X. Wang, Y. Wei et al., Mechanism for nucleation and growth of electrochemical deposition of palladium(II) on a platinum electrode in hydrochloric acid solution. *Sci. China Chem.* **57**, 755–762 (2013). <https://doi.org/10.1007/s11426-013-5026-2>
 10. Q. Zou, S. Gu, Y. Wei et al., Extraction chromatography–electrodeposition (EC–ED) process to recover palladium from high-level liquid waste. *Nucl. Sci. Tech.* **28**, 175 (2017). <https://doi.org/10.1007/s41365-017-0327-3>
 11. S.H. Lee, H. Chung, Ion exchange characteristics of palladium and rhodium from a simulated radioactive liquid waste. *J. Nucl. Sci. Technol.* **37**, 281–287 (2012). <https://doi.org/10.1080/18811248.2000.9714895>
 12. M. Ozawa, S. Koyama, T. Suzuki, nuclear rare metals and their separation in advanced ORIENT cycle strategy. *Energy Procedia* **7**, 421–424 (2011). <https://doi.org/10.1016/j.egypro.2011.06.055>
 13. E. Zambrzycka, U. Kiedysz, A.Z. Wilczewska et al., A novel ion imprinted polymer as a highly selective sorbent for separation of ruthenium ions from environmental samples. *Anal. Methods* **5**, 3096–3105 (2013). <https://doi.org/10.1039/c3ay40546j>
 14. S.Y. Ning, X.P. Wang, Q. Zou et al., Direct separation of minor actinides from high level liquid waste by Me₂-CA-BTP/SiO₂-P adsorbent. *Sci. Rep.* **7**, 14679 (2017). <https://doi.org/10.1038/s41598-017-14758-2>
 15. W. Zhang, S. Yu, S. Zhang et al., Separation of scandium from the other rare earth elements with a novel macro-porous silica-polymer based adsorbent HDEHP/SiO₂-P. *Hydrometallurgy* **185**, 117–124 (2019). <https://doi.org/10.1016/j.hydromet.2019.01.012>
 16. Q. Yu, S. Ning, Z. Wei et al., Recovery of scandium from sulfuric acid solution with a macro porous TRPO/SiO₂-P adsorbent. *Hydrometallurgy* **181**, 74–81 (2018). <https://doi.org/10.1016/j.hydromet.2018.07.025>
 17. F.W. Lewis, L.M. Harwood, M.J. Hudson et al., BTBPs versus BTPPhens: some reasons for their differences in properties concerning the partitioning of minor actinides and the advantages of BTPPhens. *Inorg. Chem.* **52**, 4993–5005 (2013). <https://doi.org/10.1021/ic3026842>
 18. R. Liu, Q. Zou, J. Zu et al., Feasibility studies on the selective separation of fission palladium(II) by isoHex-BTP/SiO₂-P adsorbent from HLLW. *J. Nucl. Sci. Technol.* **54**, 899–907 (2017). <https://doi.org/10.1080/00223131.2017.132368>
 19. Y. Wei, M. Kumagai, Y. Takashima et al., Studies on the separation of minor actinides from high-level wastes by extraction chromatography using novel silica-based extraction resins. *Nucl. Technol.* **132**, 413–423 (2000). <https://doi.org/10.13182/NT00-A3154>
 20. A. Bremer, A. Geist, P.J. Panak, Complexation of Cm(III) with 6-(5,6-dipentyl-1,2,4-triazin-3-yl)-2,2'-bipyridine studied by time resolved laser fluorescence spectroscopy. *Dalton Trans.* **41**, 7582–7589 (2012). <https://doi.org/10.1039/c2dt30541k>
 21. Y. Wei, X. Wang, R. Liu et al., An advanced partitioning process for key elements separation from high level liquid waste. *Sci. China Chem.* **55**, 1726–1731 (2012). <https://doi.org/10.1007/s11426-012-4697-4>
 22. M.J. Hudson, N. Huet, C. Madic et al., The coordination chemistry of 1,2,4-triazinyl bipyridines with lanthanide(III) elements—implications for the partitioning of americium(III). *Dalton Trans.* (2003). <https://doi.org/10.1039/B301178J>
 23. C. Dupont, C. Hill, F. Suzenet et al., Influence of an alkoxy group on bis-triazinyl-pyridines for selective extraction of americium(III). *Solv. Extr. Ion Exch.* **31**, 253–268 (2013). <https://doi.org/10.1080/07366299.2012.757160>
 24. Q. Zou, Y. Wu, Q. Shu, S. Ning, X. Wang, Y. Wei, F. Tang, Separation of palladium along with minor actinides by isoBu-BTP/SiO₂-P adsorbent from high-level liquid waste. *J. Chem. Eng. Data* **63**, 2931–2939 (2018). <https://doi.org/10.1021/acs.jced.8b00238>
 25. Y. Xu, S.-Y. Kim, T. Ito et al., Adsorption behavior of platinum group metals onto a silica-based (Crea + Dodec)/SiO₂-P extraction resin from simulated high level liquid waste. *Sep. Sci. Technol.* **50**, 260–266 (2015). <https://doi.org/10.1080/01496395.2014.956222>
 26. I.S. Kwak, S.W. Won, Y.S. Chung et al., Ruthenium recovery from acetic acid waste water through sorption with bacterial biosorbent fibers. *Bioresour. Technol.* **128**, 30–35 (2013). <https://doi.org/10.1016/j.biortech.2012.10.146>
 27. Y. Xu, S.-Y. Kim, T. Ito et al., Adsorption properties and behavior of the platinum group metals onto a silica-based (Crea + TOA)/SiO₂-P adsorbent from simulated high level liquid waste of PUREX reprocessing. *J. Radioanal. Nucl. Chem.* **297**, 41–48 (2012). <https://doi.org/10.1007/s10967-012-2314-9>
 28. A.N. Nikoloski, K.-L. Ang, D. Li, Recovery of platinum, palladium and rhodium from acidic chloride leach solution using ion exchange resins. *Hydrometallurgy* **152**, 20–32 (2015). <https://doi.org/10.1016/j.hydromet.2014.12.006>
 29. Q. Zou, R. Liu, S. Ning et al., Recovery of palladium by silica/polymer-based 2,6-bis(5,6,7,8-tetrahydro-5,8,9,9-tetramethyl-5,8-methano-1,2,4-benzotriazin-3-yl)pyridine adsorbents from high level liquid waste. *J. Nucl. Sci. Technol.* **54**, 569–577 (2017). <https://doi.org/10.1080/00223131.2017.1298481>
 30. R. Ruhela, K.K. Singh, B.S. Tomar et al., Amberlite XAD-16 functionalized with 2-acetyl pyridine group for the solid phase extraction and recovery of palladium from high level waste solution. *Sep. Purif. Technol.* **99**, 36–43 (2012). <https://doi.org/10.1016/j.seppur.2012.08.018>
 31. R. Liu, Q. Zou, J. Zu, Y. Wei, Y. Ding, Y. Zhao, Feasibility studies on the selective separation of fission palladium(II) by isoHex-BTP/SiO₂-P adsorbent from HLLW. *J. Nucl. Sci. Technol.* **54**, 899–907 (2017). <https://doi.org/10.1080/00223131.2017.1323687>
 32. D. Tiwari, H. Bhunia, P.K. Bajpai, Adsorption of CO₂ on KOH activated, N-enriched carbon derived from urea formaldehyde resin: kinetics, isotherm and thermodynamic studies. *Appl Surf Sci* **439**, 760–771 (2018). <https://doi.org/10.1016/j.apsusc.2017.12.203>
 33. Y. Dai, Y. Liu, A. Zhang, Preparation and characterization of a mesoporous polycrown impregnated silica and its adsorption for palladium from highly acid medium. *J. Porous Mater.* **24**, 1037–1045 (2016). <https://doi.org/10.1007/s10934-016-0343-4>

34. F. Li, Y. Shang, Z. Ding et al., Efficient extraction and separation of palladium (Pd) and ruthenium (Ru) from simulated HLLW by photoreduction. *Sep. Purif. Technol.* **182**, 9–18 (2017). <https://doi.org/10.1016/j.seppur.2017.03.029>
35. W. Li, W. Duan, T. Sun et al., Denitration of simulated high-level liquid waste by formic acid for the connection of PUREX process with TRPO process. *J. Radioanal. Nucl. Chem.* **314**, 221–229 (2017). <https://doi.org/10.1007/s10967-017-5357-0>
36. Y. Liu, Y. Liu, Y. Zhang, The synergistic effects of Ru and WO_x for aqueous-phase hydrogenation of glucose to lower diols. *Appl. Catal. B Environ.* **242**, 100–108 (2019). <https://doi.org/10.1016/j.apcatb.2018.09.085>
37. E. Sarica, S. Akbayrak, S. Özkaz, Ruthenium(0) nanoparticles supported on silica coated Fe_3O_4 as magnetically separable catalysts for hydrolytic dehydrogenation of ammonia borane. *Int. J. Hydrog. Energy.* **43**, 15124–15134 (2018). <https://doi.org/10.1016/j.ijhydene.2018.06.058>
38. D.J. Morgan, Resolving ruthenium: XPS studies of common ruthenium materials. *Surf. Interface Anal.* **47**, 1072–1079 (2015). <https://doi.org/10.1002/sia.5852>
39. Z. Ren, X. Xu, X. Wang et al., FTIR, Raman, and XPS analysis during phosphate, nitrate and Cr(VI) removal by amine cross-linking biosorbent. *J. Colloid Interface Sci.* **468**, 313–323 (2016). <https://doi.org/10.1016/j.jcis.2016.01.079>
40. S. Mayavan, J.-B. Sim, S.-M. Choi, Easy synthesis of nitrogen-doped graphene–silver nanoparticle hybrids by thermal treatment of graphite oxide with glycine and silver nitrate. *Carbon* **50**, 5148–5155 (2012). <https://doi.org/10.1016/j.carbon.2012.06.055>
41. A. Yoshida, W. Shen, T. Eda et al., NO_x storage/reduction over alkali-metal–nitrate impregnated titanate nanobelt catalysts and investigation of alkali metal cation migration using XPS. *Catal. Today* **184**, 78–82 (2012). <https://doi.org/10.1016/j.cattod.2011.10.018>
42. J. Dobrzyńska, R. Dobrowolski, R. Olchowski et al., Palladium adsorption and preconcentration onto thiol- and amine-functionalized mesoporous silicas with respect to analytical applications. *Microporous. Mesoporous. Mater.* **274**, 127–137 (2019). <https://doi.org/10.1016/j.micromeso.2018.07.038>
43. D.Y. Osadchii, A.I. Olivos-Suarez, A.V. Bavykina et al., Revisiting nitrogen species in covalent triazine frameworks. *Langmuir* **33**, 14278–14285 (2017). <https://doi.org/10.1021/acs.langmuir.7b02929>
44. P. Singh, M.K. Singh, Y.R. Beg et al., A review on spectroscopic methods for determination of nitrite and nitrate in environmental samples. *Talanta* **191**, 364–381 (2019). <https://doi.org/10.1016/j.talanta.2018.08.028>
45. R.D. Shannon, Revised effective ionic radii and systematic studies of interatomic distances in halides and chalcogenides. *Acta Crystallogr.* **32**, 751–767 (1976). <https://doi.org/10.1107/S0567739476001551>
46. S. Ning, W. Zhang, S. Yu et al., Selective separation of MA(III) from Ln(III) by highly stable silica-polymer-based N-donor *Isobu*-BTP/SiO₂-P adsorbent, solvent. *Extr Ion Exch* **37**, 1–14 (2019). <https://doi.org/10.1080/07366299.2019.1625998>